Research on Engineering Structures & Materials
www.jresm.org
MIM Research Group

Research Article

Multi-response optimization of 3D printing parameters for copper-loaded PLA-based nanocomposites using RSM

Mohaned S. J. Al-Suaidy [*,1,2,a], Ali Abbar Khleif [3,b], Muhsin J. Jweeg [4,c], Osama A. Q. Ziada [5,d]

[1]*Department of Smart Manufacturing, College of Production Engineering and Metallurgy, University of Technology, Iraq*
[2]*Department of Mechanical Engineering, College of Engineering, Wasit University, Iraq*
[3]*College of Mechanical Engineering, University of Technology, Iraq*
[4]*College of Technical Engineering, Al-Farahidi University, Iraq*
[5]*Department of Mechanical Engineering, Linnaeus University, Växjö, Sweden*

Article Info

Article History:

Received 24 Jun 2026

Accepted 03 Oct 2026

Keywords:

Fused deposition modeling (FDM);
Response surface methodology (RSM);
Multi-response optimization;
PLA nanocomposite;
Copper-loaded PLA;
Mechanical properties

Abstract

Fused Deposition Modeling (FDM) is widely used for functional polymer parts, yet the process-property behavior of copper-loaded filaments remains underexplored. This study maps how five FDM parameters, nozzle temperature (190-210°C), layer height (0.1-0.3 mm), infill density (20-80%), raster angle (0-90°), and print speed (40-50 mm/s), govern the ultimate tensile strength (UTS) and ultimate flexural strength (UFS) of PLActive, a commercial PLA filament containing a nano-copper additive. A face-centered central composite design of 48 runs was executed, and reduced quadratic models were fitted by backward elimination. The UTS model retained ten terms and fitted well (R^2 = 98.22%, R^2pred = 96.83%); the UFS model kept only ID, RA, and their interaction with a weaker fit (R^2 = 65.41%, R^2pred = 57.85%). Raster angle and infill density dominated both responses, with a significant ID×RA interaction ($F = 125.79$, $p < 0.001$ for UTS; $F = 6.03$, $p = 0.018$ for UFS). Desirability optimization (D = 0.921) located the optimum at ID = 80%, RA = 90°, LH = 0.3 mm, PS = 50 mm/s, with predicted UTS = 49.6 MPa and UFS = 73.6 MPa, driven by beads aligned with the applied load. Validation reached 52.0 MPa and 76.3 MPa, inside the 95% prediction band.

© 2026 MIM Research Group. All rights reserved.

1. Introduction

Fused deposition modeling (FDM) began as a rapid prototyping tool and has since grown into a reliable way to manufacture small-batch parts and components with complex geometry for the aerospace, automotive, and biomedical sectors [1]. It builds each part by laying down molten thermoplastic layer by layer, and this leaves the beads running in specific directions. The structure that results is anisotropic, so its mechanical behavior depends heavily on how the layers are oriented [2]. Because the layer-by-layer microstructure is highly sensitive to the chosen process settings, mechanical performance can vary by factors of two to four across the achievable parameter space, a sensitivity comparable in magnitude to the choice of polymer itself [3]. PLActive (Copper3D, Santiago, Chile) is a commercial PLA filament that carries a nano-copper additive and is marketed by its manufacturer as an antibacterial nanocomposite. The manufacturer reports antibacterial activity against pathogenic strains such as Staphylococcus aureus and Escherichia coli. This antibacterial function was not evaluated in the present work, which addresses mechanical performance only. This combination is useful because it gives a printed part both load-bearing

*Corresponding author: mohanedsalah@uowasit.edu.iq
[a]orcid.org/0000-0002-5979-7208; [b]orcid.org/0000-0002-1235-4493; [c]orcid.org/0000-0001-7917-9952; [d]orcid.org/0009-0008-5194-8068
DOI: http://dx.doi.org/10.17515/resm2026-1779me0624rs

capacity and, according to the manufacturer, surface antibacterial activity, which matters for items like surgical tools, orthopedic aids, and medical device housings [4]. Özen et al. [5] examined layer thickness and raster width effects on the elastic modulus and tensile strength of FDM-printed copper-reinforced PLA using multiscale modeling, restricting their analysis to two parameters and omitting flexural behavior. A Taguchi-based investigation of copper-filled metal PLA composite similarly addressed only tensile response [6]. Recent reviews of antibacterial PLA filaments [7] and biomedical PLA blends [8] have emphasized print quality and bacterial inhibition rather than structural mechanics. A combined tensile–flexural process window characterization specific to a commercial copper-loaded PLA filament of this kind is therefore currently lacking. Five process parameters are consistently identified as the principal drivers of mechanical performance in FDM: nozzle temperature, layer height, infill density, raster angle, and print speed [9,10]. Each acts through a distinct physical mechanism: melt viscosity and interlayer fusion, bead cross-section, load-bearing volume, bead alignment relative to the load axis, and cooling rate, respectively. Because these mechanisms interact, one-factor-at-a-time experiments cannot capture the interaction effects that often dominate the response surface [11]. This limitation motivates the systematic, factorial-based experimental framework employed here. Response surface methodology (RSM) offers a principled framework for such coupled systems [12]. Second-order polynomial models fitted to a designed experiment recover main effects, curvature, and two-factor interactions from a tractable number of runs. RSM has been applied to standard PLA [13,14], PETG [15], PA12-CF [16], and short fiber composites [17,18] in FDM; extending it to a commercial copper-loaded PLA filament is the focus of the present work. When multiple responses must be optimized simultaneously, the composite desirability function of Derringer and Suich combines them into a single scalar objective through the geometric mean of normalized individual desirability [19]. This framework has been adopted in FDM studies targeting tensile-flexural trade-offs [20], fatigue-efficiency balances [21], and geometry-strength objectives for biomedical scaffolds [22].

The objective of this study is to establish a statistically validated, multi-response process window for PLActive by quantifying how the five governing FDM parameters control its ultimate tensile and flexural strength, and by locating a single parameter set that maximizes both responses simultaneously. Three research questions guide the study: (i) Which process parameters and interactions most strongly govern the tensile and flexural strength of PLActive specimens? (ii) Can second-order regression models describe these relationships with useful predictive accuracy? (iii) Does a single parameter combination simultaneously maximize both UTS and UFS, or do the two responses require different settings? Addressing these questions delivers a statistically validated process window for PLActive that can inform part-level design decisions without exhaustive trial-and-error fabrication. The infill pattern was fixed as rectilinear (Lines) throughout the entire design matrix, so the present findings characterize a directionally defined internal architecture and do not extend to gyroid, honeycomb, or grid topologies [22]. All specimens were printed flat in the XY build plane; because build orientation is known to interact with raster angle in FDM [23], orientation was held constant to isolate the five selected process parameters as the sole sources of variability. Functional printed parts seldom fail under a single, pure loading mode, so a setting that strengthens one response while weakening the other is of limited use. Optimizing tensile and flexural strength together is therefore the realistic basis for selecting parameters for a load-bearing part made from this filament.

2. Materials and Experimental Procedure

2.1 Feedstock Material and Specimen Preparation

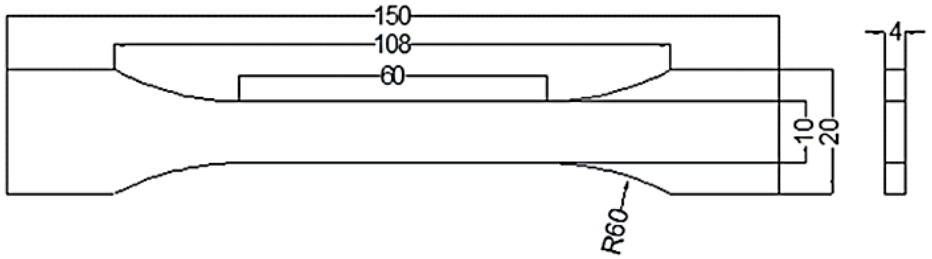
All specimens were fabricated from PLActive filament (Copper3D, Santiago, Chile), 1.75 ± 0.05 mm in diameter, a PLA-based filament that its manufacturer markets as an antibacterial nanocomposite. PLA was selected for its biodegradability and biocompatibility [24], while the dispersed copper phase is the basis of the manufacturer-reported antibacterial functionality, which was not evaluated in this study. Before each printing session, the spools were stored in a sealed desiccator at 25 °C and below 30 % relative humidity for at least 24 h. Moisture absorption in PLA-based filaments can produce inconsistent melt flow, bubble formation, and sub-surface voids that

introduce scatter into mechanical test results [25,26]. Material composition and fixed machine settings are summarized in Table 1 (material values compiled from the manufacturer's technical and safety data sheets [27]). According to the safety data sheet, the filament consists of polylactide resin (> 99 wt.%) and less than 1 wt.% of a nano-copper additive, NanoCu PCZ001, in which a zeolite 4A carrier (75 %) holds copper hydroxyacetate (25 %). The technical data sheet reports that two independent microbiology laboratories, in the USA and in Chile, measured a reduction of more than 99.99 % in the colony-forming units of methicillin-resistant Staphylococcus aureus and Escherichia coli after 24 h of exposure, and it lists a recommended print window (190–210 °C, 40–50 mm/s, layer height ≥ 0.1 mm) that the nozzle-temperature and print-speed levels in Table 2 follow [27]. These antibacterial data are the manufacturer's; the present study neither tests them nor relies on them.

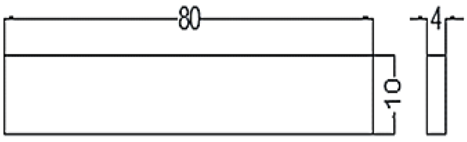
Table 1. PLActive material properties and fixed printer settings

Parameter	Specification
Matrix	Polylactide resin (> 99 wt.%)
Additive	Nano-copper additive NanoCu PCZ001, < 1 wt.% (zeolite 4A 75%, copper hydroxyacetate 25%)
Filament diameter	1.75 ± 0.05 (mm)
Recommended nozzle temperature	190–210 (°C)
Glass transition temperature (Tg)	55-60 (°C)
Density	~1.24 (g/cm^3)
FDM printer	Bambu Lab X1E (closed chamber, 0.4 mm nozzle)
Bed temperature	45 °C (constant across all runs)
Infill pattern	Rectilinear (Lines) as a fixed factor in this study
Perimeter walls	3
Cooling fan	80% (activated from layer 3)

Tensile specimens followed the ISO 527-2 type 1B geometry (150 mm overall length, 50 mm gauge length, 10 mm width, 4 mm nominal thickness), Fig. 1(a). Flexural specimens were 80 × 10 × 4 mm with a 16:1 span-to-depth ratio, in accordance with ASTM D790 three-point bending, Fig. 1(b). All specimens were printed flat in the XY build plane to maintain consistent bead orientation relative to the loading axis across the 48-run matrix. Build orientation is known to interact with raster angle in FDM [23], and fixing it to the XY plane isolates the five selected process parameters as the sole drivers of variability.



(a)



(b)

Fig. 1. Specimen geometry: (a) ISO 527-2 type 1B tensile; (b) ASTM D790 flexural specimen

2.2 Mechanical Testing

All tests were performed on an MTS Exceed Model E45 electro-mechanical universal testing machine at 23 ± 2 °C and 50 ± 5 % relative humidity, with a crosshead speed of 0.100 mm/s and a

data acquisition rate of 5.0 Hz. The same operator, fixture, and machine were used throughout the 48-run matrix to control inter-operator and inter-setup variance [28]. A single constant crosshead rate of 0.100 mm/s (6 mm/min) was applied to both the tensile and flexural tests so that the loading kinematics were identical across the 48-run matrix; for the 64 mm flexural span used here, this rate lies within the interval bracketed by ASTM D790 Procedures A and B, and its uniform application means any rate-dependence of PLA is common to all runs.

For tensile tests, the ultimate tensile strength was calculated from the peak engineering stress before fracture, as given in Eq. (1):

$$\sigma_{UTS} = \frac{P_{max}}{A_0} \tag{1}$$

where σ_{UTS} is the ultimate tensile strength (MPa), P_{max} is the peak tensile load (N), and A_0 is the initial gauge cross-sectional area (width × thickness = 10 × 4 = 40 mm^2). A_0 is the nominal external cross-section, so the reported strengths are apparent (engineering) values for that section; every specimen had a fixed three-wall perimeter, with rectilinear infill varied as a design factor, and the strengths are therefore apparent values at the specified infill rather than true solid-material stress.

For flexural tests, the UFS was calculated from the standard three-point bending expression Eq. (2):

$$\sigma_{UFS} = \frac{3P_{flex}\,L}{2bd^2} \tag{2}$$

where σ_{UFS} is the ultimate flexural strength (MPa), P_{flex} is the peak bending load (N), L is the support span (mm), b is the specimen width (10 mm), and d is the thickness (4 mm).

3. Experimental Design

The experimental matrix was built on a five-factor Face-centered Central Composite Design (FCCD). The design comprised 32 factorial runs (2^5), 10 axial runs at α = 1.0, and 6 center-point replicates, giving a total of 48 runs [7,29]. Setting α = 1.0 keeps every factor level inside the range that was physically tested, which suits the fairly narrow print window recommended for PLActive. The six center-point replicates provide the pure error estimate for the ANOVA lack of fit test and allow detection of curvature in the response [30]. The 32 factorial and 10 axial runs were single specimens; only the center point was replicated, so the pure-error estimate rests on the center, which is the conventional face-centered CCD structure. All 48 runs were carried out in a fully randomized order to mitigate systematic bias from environmental drift or batch variability.

The coded and actual levels of the five FDM parameters are given in Table 2, and the full 48-run matrix with the measured UTS and UFS responses is presented in Table 3. The measured UTS values ranged from 13.45 to 50.38 MPa (a 3.7-fold span), and the UFS values from 12.23 to 83.22 MPa (a 6.8-fold span) [30]. The larger UFS spread is consistent with the geometry-sensitive nature of three-point bending failure. At the center-point condition, the coefficient of variation across the six replicates was 1.1 % for UTS and 10.4 % for UFS. These low replicate variations indicate that the wide response ranges observed across the design space are driven by parameter effects rather than experimental noise.

Table 2. FDM process parameters and their coded and actual levels

Factor	Symbol	Unit	Low (−1)	Center (0)	High (+1)
Nozzle Temperature	NT	°C	190	200	210
Layer Height	LH	mm	0.1	0.2	0.3
Infill Density	ID	%	20	50	80
Raster Angle	RA	°	0	45	90
Print Speed	PS	mm/s	40	45	50

Table 3. FCCD experimental matrix and corresponding UTS and UFS responses

Run Order	Nozzle Temp (degree)	Layer Height (mm)	Infill Density (%)	Raster Angle (degree)	Print Speed (mm/s)	UTS (MPa)	UFS (MPa)
1	190	0.1	20	0	40	16.773	30.560
2	190	0.2	50	45	45	27.006	48.652
3	190	0.1	80	0	50	18.245	26.266
4	190	0.3	80	90	50	49.375	79.382
5	200	0.2	80	45	45	29.222	60.421
6	200	0.1	50	45	45	26.461	45.740
7	210	0.3	80	90	50	50.375	80.114
8	190	0.1	80	90	40	48.878	68.599
9	210	0.3	20	0	40	27.852	39.664
10	200	0.2	50	45	45	26.027	49.518
11	190	0.3	20	0	50	24.811	35.090
12	210	0.3	80	90	40	47.390	71.713
13	190	0.3	20	90	50	35.313	52.840
14	210	0.1	20	90	50	30.653	57.530
15	190	0.3	80	90	40	47.302	71.309
16	210	0.3	20	90	40	35.921	57.892
17	190	0.1	80	90	50	48.302	65.416
18	200	0.2	50	45	45	25.800	41.335
19	210	0.3	80	0	50	28.376	56.346
20	200	0.2	50	45	45	25.858	50.163
21	210	0.3	20	0	50	23.999	49.570
22	190	0.1	20	90	50	29.940	41.195
23	210	0.1	20	0	40	17.840	27.433
24	210	0.2	50	45	45	24.599	45.018
25	210	0.1	80	0	50	22.338	59.772
26	210	0.1	80	90	40	48.362	73.974
27	190	0.3	20	0	40	24.259	36.351
28	200	0.2	50	45	45	25.667	40.454
29	210	0.3	80	0	40	27.971	42.692
30	200	0.2	50	45	45	25.166	42.162
31	190	0.1	20	90	40	28.881	38.582
32	190	0.3	80	0	40	27.548	36.992
33	200	0.2	20	45	45	23.795	42.030
34	200	0.2	50	45	45	25.756	40.424
35	210	0.3	20	90	50	35.673	58.580
36	200	0.2	50	90	45	38.338	59.851
37	200	0.2	50	45	50	24.811	34.248
38	200	0.3	50	45	45	30.285	52.997
39	210	0.1	80	90	50	48.846	83.216
40	190	0.3	80	0	50	31.531	36.187
41	190	0.3	20	90	40	35.977	51.333
42	200	0.2	50	0	45	22.884	54.210
43	210	0.1	20	90	40	29.537	39.356
44	210	0.1	80	0	40	21.797	33.449
45	200	0.2	50	45	40	24.483	63.407
46	210	0.1	20	0	50	14.840	12.291
47	190	0.1	80	0	40	18.291	12.226
48	190	0.1	20	0	50	13.451	17.529
Overall mean ± SD: UTS = 29.93 ± 9.93 MPa | UFS = 48.21 ± 16.70 MPa							

4. Statistical Modeling and Analysis of Variance

4.1 UTS Regression Model

A second-order polynomial was fitted to the UTS data and reduced by stepwise backward elimination. This started from twenty terms: five linear, five squared, and ten two-factor interactions. The term carrying the highest p-value was dropped at each step, and the procedure was repeated until only significant terms remained. Nozzle temperature (NT) was the first to go, and once removed, it never re-entered the model. The retained model, with linear main effects kept for hierarchical completeness [31], is given in Eq. (3):

$$UTS = 21.12 - 12.7 \cdot LH - 0.0515 \cdot ID - 0.0206 \cdot RA - 0.179 \cdot PS + 179.1 \cdot LH^2 + 0.001990 \cdot RA^2 - 0.2821 \cdot LH \cdot ID - 0.3392 \cdot LH \cdot RA + 0.002191 \cdot ID \cdot RA + 0.003790 \cdot ID \cdot PS \quad (3)$$

The negative coefficient on ID does not imply that higher infill density reduces tensile strength. Its effect is reversed by the positive ID×RA interaction: at RA = 90° the interaction term dominates, and UTS rises with ID, while at RA = 0° the interaction effectively vanishes. Eq. (3) is written in uncoded units for prediction; the term-level significance in Table 4 is assessed on the coded (−1, 0, +1) model, which removes the correlation between the linear terms and their squares and interactions that otherwise mask the main-effect significance. Model performance: R^2 = 98.22%, R^2(adj) = 97.74%, R^2(pred) = 96.83%, and S = 1.49 MPa. The narrow gap between R^2 and R^2(pred) indicates the model is not overfitted [32]. Comparable predictive accuracy has been reported for RSM models of FDM tensile strength in PLA composites [33,34].

The ANOVA for the UTS regression is given in Table 4. The overall regression is highly significant (F = 204.29, p < 0.001), with raster angle being the largest single contributor (about 60.7% of the regression sum of squares) and the ID×RA interaction contributing 6.2% (F = 125.79, p < 0.001). The lack-of-fit test returns p = 0.001, driven by the very small pure error estimate from the center-point replicates (CV = 1.1%). A similar pattern is widely observed in high-precision FDM RSM studies [35,36], and does not in itself invalidate the regression.

Table 4. ANOVA for the UTS second-order regression model (computed on the coded model)

Source	DF	Adj SS	Adj MS	F-Value	P-Value
Regression	10	4548.07	454.81	204.29	< 0.001
LH	1	297.20	**297.20**	133.52	< 0.001
ID	1	797.19	797.19	358.13	< 0.001
RA	1	2758.63	2758.63	1239.28	< 0.001
PS	1	0.10	0.10	0.04	0.836
LH^2	1	11.54	11.54	5.18	0.029
RA^2	1	58.38	58.38	26.22	< 0.001
LH × ID	1	22.92	22.92	10.29	0.003
LH× RA	1	74.56	74.56	33.49	< 0.001
ID × RA	1	280.04	280.04	125.79	< 0.001
ID × PS	1	10.36	10.36	4.65	0.038
Error	37	82.37	2.23	—	—
Lack-of-Fit	32	81.94	2.56	29.71	0.001
Pure Error	5	0.43	0.09	—	—
Total	47	4630.44	—	—	—

Notes: R^2 = 98.22 %, R^2(adj) = 97.74 %, R^2(pred) = 96.83 %, S = 1.49 MPa. Term-level statistics computed on the coded model; main effects retained for hierarchy.

4.2 UFS Regression Model

The same backward elimination procedure was applied to the UFS data, with all 48 runs included in the fit. The retained model is sparser than for UTS: only ID, RA, and their interaction were significant, and it is given in Eq. (4):

$$UFS = 29.24 + 0.1181 \cdot ID + 0.1272 \cdot RA + 0.003260 \cdot ID \cdot RA \quad (4)$$

The model achieved R^2 = 65.41 %, R^2(adj) = 63.05 %, and S = 10.15 MPa. The overall regression is statistically significant (F = 27.74, p < 0.001). The Type II ANOVA partition (Table 5) confirms that the ID×RA interaction is significant at the α = 0.05 level (F = 6.03, p = 0.018); in coded units, both main effects are significant in their own right (ID: F = 20.85; RA: F = 56.33) and together contribute most of the regression sum of squares. The UFS R^2 of 65.41 % is far below the 98.22 % for UTS. In three-point bending, failure concentrates beneath the loading nose, where localized voids, bead-junction defects, and interlayer heterogeneities dominate. These are not captured by the global process parameters [2,37], and R^2 of 60-75% is common for second-order UFS models in PLA-based FDM [38]. With a prediction interval near ±22 MPa at the optimum, the model suits ranking and trend identification, not point design values without verification.

Table 5. ANOVA for the UFS second-order regression model (Computed on the coded model)

Source	DF	Adj SS	Adj MS	F-Value	P-Value
Regression	3	8573.8	2857.9	27.74	< 0.001
ID	1	2148.06	2148.06	20.85	< 0.001
RA	1	5804.75	5804.75	56.33	< 0.001
ID × RA	1	621.0	621.0	6.03	0.018
Error	44	4533.8	103.0	—	—
Lack-of-Fit	39	4429.6	113.6	5.45	0.033
Pure Error	5	104.3	20.9	—	—
Total	47	13107.6	—	—	—

Notes: R^2 = 65.41 %, R^2(adj) = 63.05 %, S = 10.15 MPa. Term-level statistics computed on the coded model.

5. Results and Discussion

5.1 Main Effects

Fig. 2 shows the main effect plots for UTS and UFS. Each panel reports the mean response at each factor level while the remaining factors are held at their center values; the dashed line marks the overall mean (UTS = 29.93 MPa; UFS = 48.21 MPa). The two responses move in physically consistent directions. UTS rises strongly with raster angle (22.5-40.5 MPa, +80%) and with infill density (26.4-36.1 MPa, +37%). At a 90° raster, the perimeter walls and inner roads are aligned with the tensile axis, so the load is carried through the stiffer extrusion direction; the aligned inner raster provides a continuous secondary load path [39,40]. Layer height adds a smaller but steady gain, raising UTS from 28.4 to 34.4 MPa as LH goes from 0.1 to 0.3 mm (+21%); the thicker beads have larger cross-sections, so neighboring beads fuse more completely. Print speed has no significant main effect (p = 0.836). It enters only through its interaction with infill density (ID×PS, p = 0.038). Nozzle temperature barely moves UTS across 190–210 °C, the print window recommended for PLActive. The same two factors dominate the UFS plots. Mean UFS rises from 35.7 MPa at 0° raster to 61.8 MPa at 90° (+73 %), and from 40.5 MPa at 20 % infill to 56.4 MPa at 80 % (+39 %). Layer height, print speed, and nozzle temperature produce negligible flexural main effects. This is consistent with the bending mechanics: in three-point bending, the stress field is governed primarily by cross-sectional geometry and bead orientation rather than by the thermal history of each road [41]. Because flexural response scatters more, these UFS trends are read as directional rankings rather than as design values.

5.2 Interaction Effects and Response Surfaces

Fig. 3 illustrates the strong ID×RA interaction in the UTS model. In panel (a), at 0° raster (filaments perpendicular to the loading axis), UTS rises by only about 4 MPa as infill density increases from 20 % to 80 %. The rate-limiting mechanism at this orientation is rupture of the inter-raster bonds; adding more material of the same kind does not strengthen the part substantially. At a 90° raster, the same change in infill drives UTS up by approximately 16 MPa, because the internal bead network now aligns with the loading axis and each additional unit of infill widens the load-bearing cross-section [42].

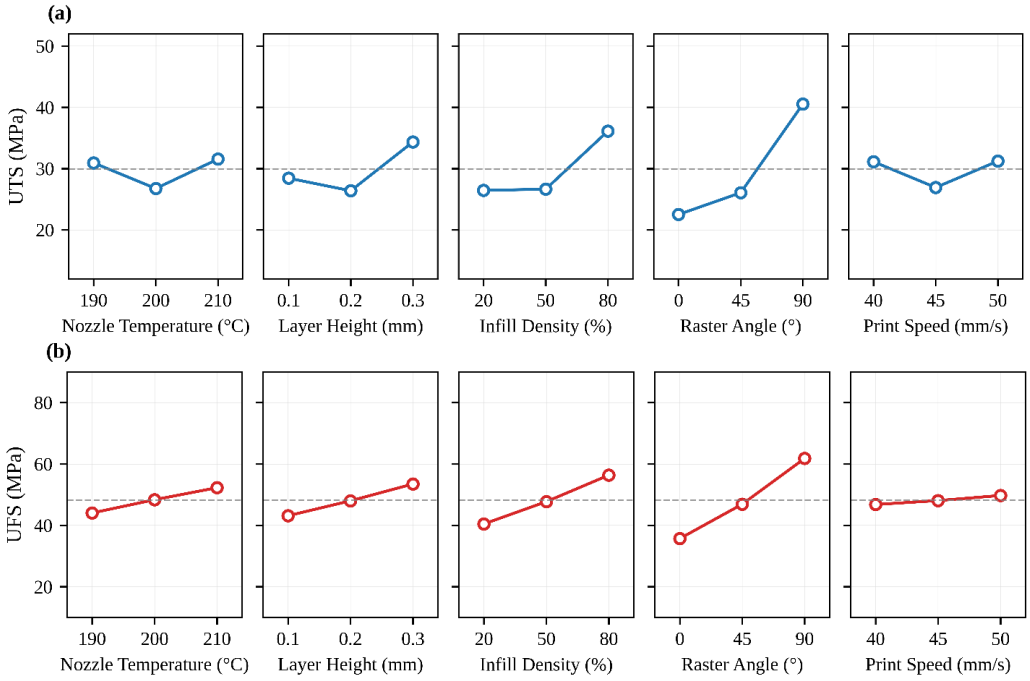


Fig. 2. Main effects plots for (a) UTS (top row), and (b) UFS (bottom row)

Thicker beads (LH×RA, Fig. 3b) raise UTS at 90° by enlarging the load-bearing columns but have a negligible effect at 0°, where the inter-raster bond governs; the LH×ID coupling (Fig. 3c) is weaker still. The interactions converge on a single mechanism: the strength of PLActive is set by the alignment of the load-bearing bead columns with the principal stress direction, consistent with the ID×RA coupling reported for unreinforced PLA, wood–PLA biocomposites, and short-fiber-reinforced PLA [20, 24, 26].

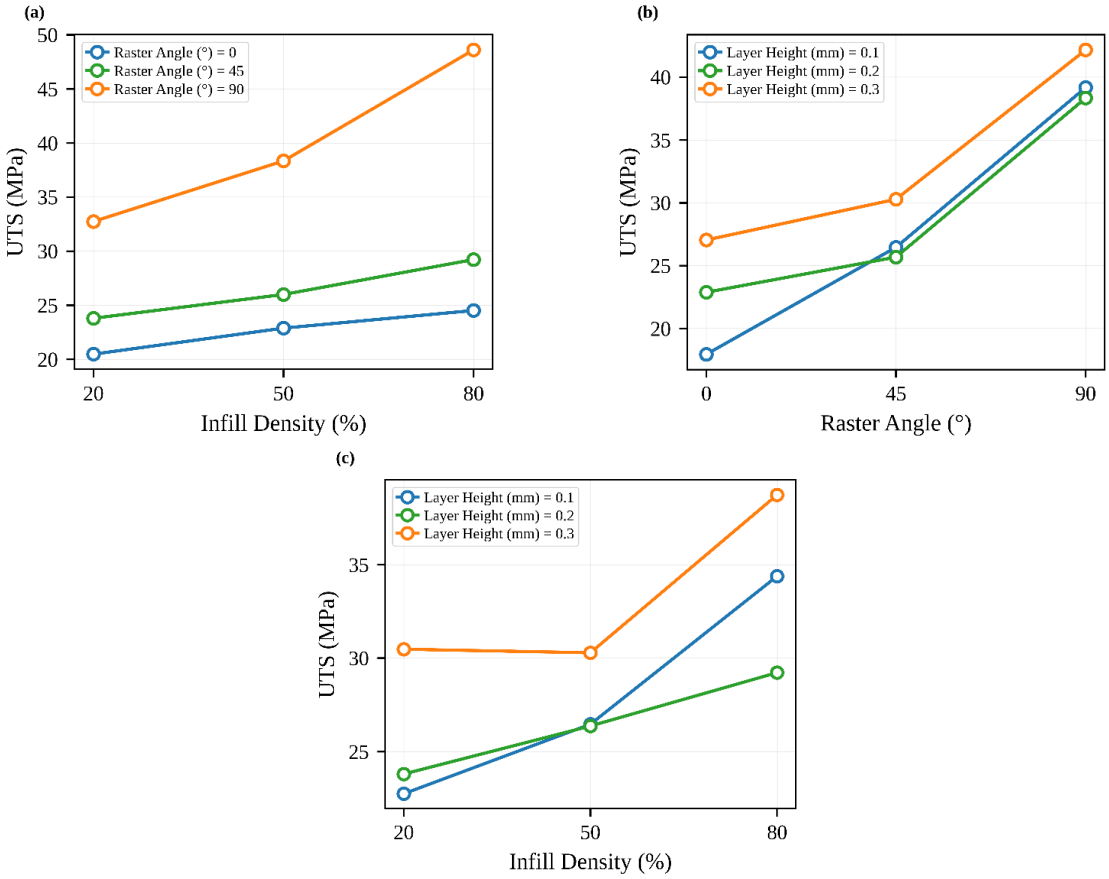


Fig. 3. Two-factor interaction plots for UTS: (a) ID × RA; (b) RA × LH; (c) ID × LH

The contour maps in Fig. 4 cover the ID×RA design space at fixed LH = 0.3 mm and PS = 50 mm/s. The two responses peak in the same corner: high infill (80 %) and high raster angle (90°). The absence of a trade-off between UTS and UFS in this region is the reason a single corner optimum can be reached, as developed in Section 6. Both maps are plotted against infill density and raster angle, and the black star (★) marks the optimal parameter combination (D = 0.921).

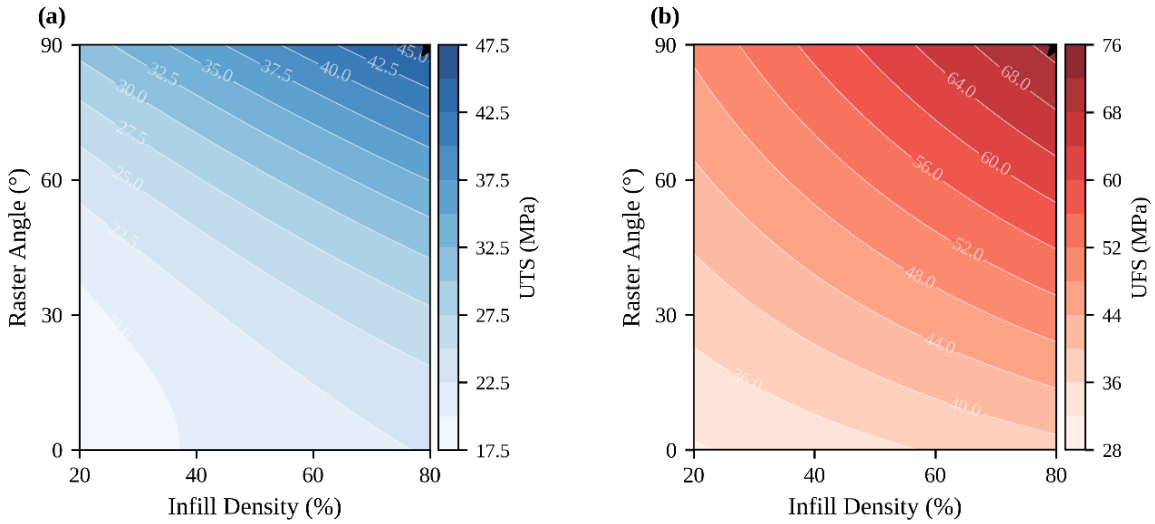


Fig. 4. Contour plots showing (a) UTS and (b) UFS

5.3 Factor Contributions and Model Diagnostics

Fig. 5(a) ranks the UTS model terms by their adjusted sum of squares. Raster angle is the dominant contributor (F = 1239.28), followed by infill density (F = 358.13) and layer height (F = 133.52); among the two-factor terms, ID×RA leads (F = 125.79, p < 0.001), ahead of LH×RA (F = 33.49), with RA^2 (F = 26.22) the leading curvature term. Each of the remaining terms accounts for a much smaller share of the regression. In practical terms, the optimization of PLActive tensile strength is largely a two-parameter problem once ID and RA are chosen correctly [9].

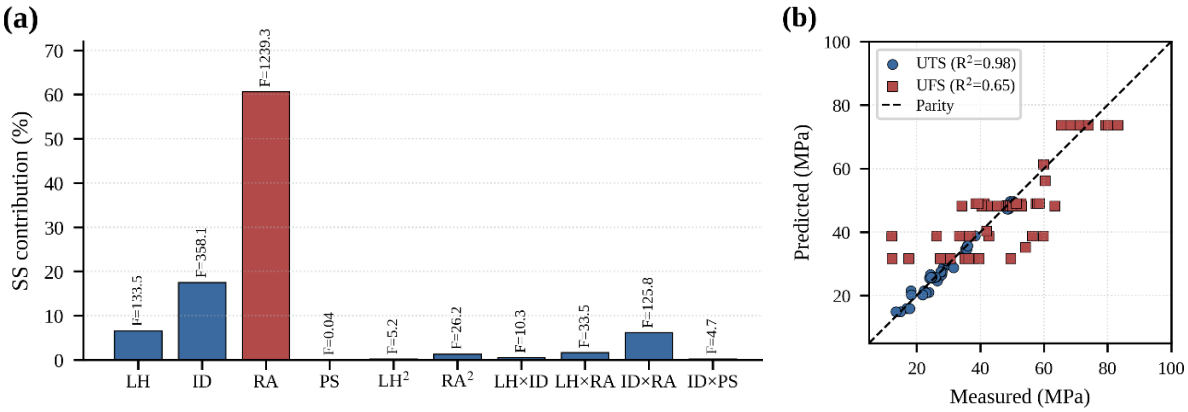


Fig. 5. Model diagnostics: (a) contribution of each term to the UTS model variance; (b) predicted against measured strength for the UTS and UFS models over the 48 design runs

Fig. 5(b) plots measured against model-predicted values for both responses. The UTS points sit close to the parity line (R^2 = 0.98). The UFS cloud is visibly broader (R^2 = 0.65), a difference that reflects the larger stochastic component of bending failure in FDM specimens. The broader UFS scatter is comparable to that reported for second-order UFS regressions of PLA and PLA composite filaments in the recent literature [15,18]. The prominence of the ID×RA interaction as the leading two-factor term in both responses matches the behavior reported for unreinforced PLA, wood–PLA biocomposites, and short-fiber-reinforced PLA [16,20,26], where alignment of the bead network with the loading direction at high raster angles is well established [39,40]; within the mechanical-

testing scope of this study, no additional interaction or mechanism specific to the copper-bearing additive was detected. The UTS accuracy (R^2 = 98.22%, R^2(pred) = 96.83%) sits at the upper end of FDM RSM studies, where values between 90% and 96% are more typical [36,37]. Two factors plausibly contribute: the wide 20–80% infill range used in the FCCD resolves the dominant ID×RA nonlinearity more cleanly than the narrower windows used in earlier work, and PLActive remains thermally stable across the 190–210°C window, which limits batch-to-batch variability in filament fusion, a typical source of noise in FDM mechanical data [25,26].

6. Multi-Response Optimization

6.1 Composite Desirability Approach

Balancing the two strengths in a single parameter set calls for the Derringer–Suich composite desirability function, which was applied here for that purpose [19]. Equation (5) maps each response onto its own desirability score d_i between 0 and 1, and Equation (6) merges the two scores by taking their geometric mean. The two responses were weighted equally (w = 1), since no service requirement here favors tension over bending or the other way around. For the bounds, the experimental extremes were used directly: 13.45 to 50.38 MPa for UTS and 12.23 to 83.22 MPa for UFS. Using the geometric mean matters because it drives the combined score toward zero whenever either response performs poorly, so a high D can only come from a setting that does reasonably well on both at once [19].

$$d_i = \frac{y_i - y_{i,min}}{y_{i,max} - y_{i,min}} \quad (5)$$

Where d_i is the individual desirability, y_i is the predicted response value, and $y_{i,min}$ and $y_{i,max}$ are the lower and upper bounds, respectively.

$$D = \sqrt{(d_{UTS} \times d_{UFS})} \quad (6)$$

Where D represents the composite desirability for the two mechanical responses.

6.2 Optimal Settings and Predicted Performance

The optimization outcome is summarized in Table 6. The composite desirability converges to a single corner of the design space ID = 80 %, RA = 90°, LH = 0.3 mm, PS = 50 mm/s, with nozzle temperature defaulting to the 200 °C center, because it has no significant effect across 190–210 °C. The corresponding individual desirability is d(UTS) = 0.980 and d(UFS) = 0.865, giving a composite D = 0.92. Predicted strengths at this setting are UTS = 49.6 MPa and UFS = 73.6 MPa. The flexural figure is a trend-level estimate; given its wide prediction interval (Table 6), it should guide ranking rather than serve as a point design value.

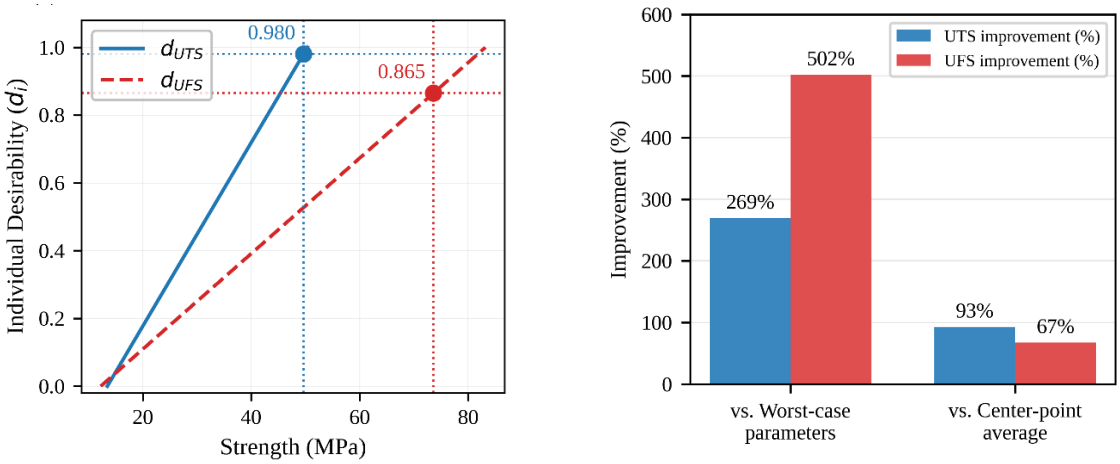
The agreement between the predicted optimum and the closest experimental runs (Runs 4 and 7, printed at the optimal ID, RA, LH, and PS and differing only in nozzle temperature) is within 1–2 % for UTS and within 7–9 % for UFS. This level of agreement is consistent with similarly structured RSM-based optimization studies in FDM [14,22]. The predicted optimum UTS of 49.6 MPa lies within the range typically reported for optimized PLA-based parts in FDM [33,34]. The multiscale modeling study on copper-reinforced PLA by Özen et al. [5] returned UTS values of comparable magnitude, although their design covered only two factors. The predicted UFS of 73.6 MPa falls within the 60–80 MPa range frequently quoted for unreinforced PLA in three-point bending [41]. These comparisons concern magnitude only; without a neat-PLA control, no strength effect is attributed to the copper-bearing additive. Nozzle temperature does not exhibit a statistically significant effect within the tested range (190–210 °C); the optimizer, therefore, defaults to the center-point value. The negligible nozzle-temperature effect across 190–210 °C indicates reliable filament fusion throughout the manufacturer-recommended window, leaving the operator a practical margin around 200 °C. This conclusion is range-specific; behavior at wider spans (for example, 170–230 °C), where degradation of the copper-bearing phase could intervene, was not investigated. A further limitation is that no microstructural characterization (SEM, micro-CT) was carried out, so the attribution of the residual UFS scatter to voids and bead-junction heterogeneity, and the absence of a detectable mechanistic contribution from the copper phase, rests on the

mechanical data alone. Complementary imaging or thermal analysis (TGA/DSC) is recommended to resolve these questions in future work.

Fig. 6 presents the optimization outcome graphically. Panel (a) shows the individual desirability curves for UTS and UFS, with the dashed lines marking the predicted optimal values; both fall close to the upper bounds of their respective ranges. Panel (b) expresses the optimum as practical strength improvements. Compared with the worst run in the matrix, the optimal setting raises UTS by 269 % and UFS by 502 %. Compared with the center point average, a reasonable reference for default print settings, the optimal corner returns +93 % for UTS and +67 % for UFS. These improvements arise from a deliberate exploitation of the ID × RA synergy rather than from any change in the underlying process technology.

Table 6. Optimal 3D printing parameters and model predictions at D = 0.921

Parameter	Optimal value	Response	Predicted	95% CI	95% PI
Infill Density	80%	UTS	49.645 MPa	[48.07, 51.23]	[46.23, 53.06]
Raster Angle	90°	UFS	73.630 MPa	[66.82, 80.44]	[52.07, 95.19]
Layer Height	0.3 mm	d(UTS)	0.980	—	—
Print Speed	50 mm/s	d(UFS)	0.865	—	—
Nozzle Temp.	200 °C (center)	Composite D	0.921	—	—



(a) (b)

Fig. 6. Desirability analysis and performance gains: (a) Individual desirability functions (di) for UTS and UFS, where dashed lines indicate predicted optima; (b) Percentage strength improvement at the optimal settings (D = 0.921) relative to worst-case and center-point reference conditions

6.3 Experimental Validation of the Predicted Optimum

To check whether the predicted corner survives outside the model, the optimal setting was printed and tested directly. Specimens were produced at the optimum (NT = 200 °C, LH = 0.3 mm, ID = 80 %, RA = 90°, PS = 50 mm/s) on the same machine and fixture used for the design matrix, and each response was measured in triplicate. The tensile strength averaged 52.0 ± 0.8 MPa and the flexural strength 76.3 ± 1.1 MPa (Table 7). Both means fall inside the 95 % prediction intervals reported in Table 6, and the standard deviation across the three repeats stays close to 1 MPa, which points to a repeatable print at this corner.

The measured tensile mean sits about 4.8 % above the predicted 49.6 MPa, and the flexural mean about 3.7 % above 73.6 MPa. A small positive offset of this size is what tends to show up when the optimum lands on a design boundary, since the quadratic surface rounds off part of the steep gain that aligned rasters give right at RA = 90°, leaving the printed parts a little stronger than the fitted value rather than weaker. The flexural agreement is the tighter of the two, even though the UFS model carried the weaker overall fit, so the larger UFS scatter seen across the full design seems to sit away from this corner rather than on it. Neither response opens the kind of gap that would hint

at a missing term or an unmodeled effect at the optimum, and the confirmation runs support using this setting as the recommended operating point for PLActive. For reference, the manufacturer lists a tensile strength at break of 53 MPa, a tensile yield strength of 60 MPa, and a flexural strength of 83 MPa as typical values for injection-molded amorphous bars [27]. The confirmed printed values at the optimum therefore reach about 98 % (break) and 87 % (yield) of the molded tensile values and about 92 % of the molded flexural strength, which places the optimized prints close to the bulk reference.

Table 7. Experimental validation of the predicted optimum against confirmation specimens (mean of three repeats)

Response	Predicted (MPa)	95 % PI (MPa)	Measured mean ± SD (MPa)	Deviation (%)
UTS	49.645	[46.23, 53.06]	52.03 ± 0.78	+4.8
UFS	73.630	[52.07, 95.19]	76.33 ± 1.05	+3.7

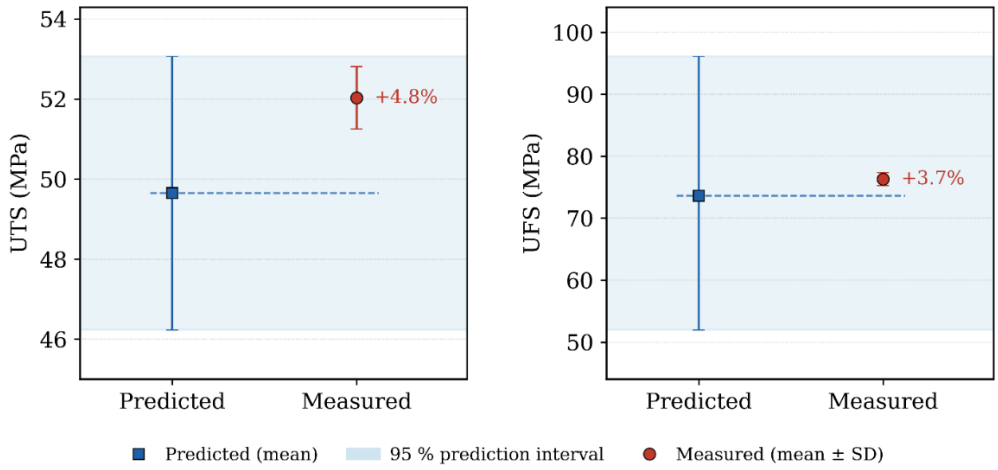


Fig. 7. Experimental validation at the predicted optimum for the tensile (left) and flexural (right) strength. The shaded band is the 95 % prediction interval; the square marks the model prediction, and the circle the measured mean of three confirmation specimens with ±1 SD

7. Conclusions

This study presents a statistically structured characterization of FDM process effects on the tensile and flexural strength of PLActive, a copper-loaded PLA filament that its manufacturer markets as antibacterial. The main outcomes are summarized as follows. In direct answer to the three research questions, (i) infill density and raster angle, acting together, most strongly govern both strengths, while nozzle temperature is statistically inert, layer height affects UTS moderately, and print speed shows no significant main effect; (ii) the second-order UTS model predicts within the design space with high accuracy (R^2pred = 96.83%), whereas the UFS model captures the same directional pattern but should be read as a trend indicator; and (iii) a single corner of the design space maximizes both responses because UTS and UFS share the same optimum rather than pulling in opposite directions.

- The second-order UTS regression achieved high predictive accuracy (R^2 = 98.22 %, R^2(adj) = 97.74 %, R^2(pred) = 96.83 %, S = 1.49 MPa). Within the design space studied, the model is accurate enough to be used for point prediction.
- The UFS regression kept only ID, RA, and their interaction, and its fit was moderate (R^2 = 65.41%, R^2adj = 63.05%, S = 10.15 MPa). It points to the same directional trend that dominates UTS, but its predicted values are better read as indicators of the trend than as numbers to design from.
- Infill density and raster angle are the principal drivers of both responses, acting through a significant ID×RA interaction (F = 125.79, p < 0.001 for UTS; F = 6.03, p = 0.018 for UFS).

Within the mechanical testing scope of this study, no additional mechanism specific to the copper-bearing additive was detected; this inference is supported by the mechanical data alone, and resolving any mechanistic role of the copper phase would require complementary microstructural or thermal characterization.

- Multi-response optimization by composite desirability identified a single corner condition (ID = 80 %, RA = 90°, LH = 0.3 mm, PS = 50 mm/s) at D = 0.92, with predicted UTS = 49.6 MPa and UFS = 73.6 MPa. The optimum delivers strength gains of approximately +93 % (UTS) and +67 % (UFS) relative to the center-point reference. Confirmation prints at this corner returned 52.0 MPa in tension and 76.3 MPa in bending, both inside the 95 % prediction intervals, so the optimum holds under direct test.

Nozzle temperature showed no statistically significant effect across 190-210 °C, which leaves the operator some freedom to work anywhere within the manufacturer's recommended print window. Taken together, these results give a compact, statistically grounded process window for a commercial copper-bearing PLA filament. For a load-bearing part, printing at 80 % infill with a 90° raster, 0.3 mm layers, and 50 mm/s gives the best simultaneous tensile and flexural performance, and the small deviation between the predicted and confirmed strengths (about 5 % and 4 %) shows the corner is reproducible in practice. The antibacterial activity of PLActive is reported by the manufacturer [27] and was not evaluated here; testing it on printed specimens is planned as follow-up work, and because no neat-PLA control was printed, the measured strengths are not attributed to the copper phase; separating any copper-specific mechanical contribution would need a neat-PLA baseline together with microstructural and thermal characterization. The analysis route itself is not tied to this filament: the same face-centered design, coded-unit ANOVA, and desirability optimization can be applied to other functional filaments to locate their own tensile–flexural process windows from a modest number of runs. Whether the ID×RA behavior reported here carries over to other infill topologies and to other build orientations is left open for future work, alongside the micro-CT, SEM, or thermal characterization needed to connect the residual UFS scatter to specific defect populations.

References

[1] Siyoum YB, Kindie FG, Gebeyehu MA. A review of current research and prospects of fused deposition modelling: application, materials, performance, process variables, parameter optimization, and numerical study. Int J Adv Manuf Technol. 2025;138:1675-1711. https://doi.org/10.1007/s00170-025-15615-7

[2] Moradi M, Moghadam MK, Shamsborhan M, Bodaghi M. The synergic effects of FDM 3D printing parameters on mechanical behaviors of bronze poly lactic acid composites. Journal of Composites Science. 2020;4(1). https://doi.org/10.3390/jcs4010017

[3] Kamaal M, Anas M, Rastogi H, Bhardwaj N, Rahaman A. Effect of FDM process parameters on mechanical properties of 3D-printed carbon fibre-PLA composite. Progress in Additive Manufacturing. 2021;6(1):63-69. https://doi.org/10.1007/s40964-020-00145-3

[4] Alazzawi S, Ali NH, Shihab SK, Hanon MM. Investigating the impact of process parameters on the thermomechanical properties of three-dimensional (3D) printed polymer-nanoclay composites. International Journal of Thermofluids. 2025;27. https://doi.org/10.1016/j.ijft.2025.101168

[5] Özen A, Ganzosch G, Völlmecke C, Auhl D. Characterization and Multiscale Modeling of the Mechanical Properties for FDM-Printed Copper-Reinforced PLA Composites. Polymers (Basel). 2022;14(17). https://doi.org/10.3390/polym14173512

[6] Kyratsis V, Tzotzis A, Korlos A, Efkolidis N. Investigation of the Fabrication Parameters' Influence on the Tensile Strength of 3D-Printed Copper-Filled Metal Composite Using Design of Experiments. Journal of Manufacturing and Materials Processing. 2024;8(6). https://doi.org/10.3390/jmmp8060278

[7] Khan I, et al. Investigation and Optimization of Processing Parameters Affecting the Mechanical Properties of Carbon Particle-Reinforced Thermoplastic Polyurethane Samples Fabricated via Fused Filament Fabrication. J Mater Eng Perform. 2025;34(23):28331-28341. https://doi.org/10.1007/s11665-025-11154-0

[8] Morvayová A, Contuzzi N, Fabbiano L, Casalino G. Multi-Attribute Decision Making: Parametric Optimization and Modeling of the FDM Manufacturing Process Using PLA/Wood Biocomposites. Materials. 2024;17(4). https://doi.org/10.3390/ma17040924

[9] Abas M, Habib T, Noor S, Salah B, Zimon D. Parametric Investigation and Optimization to Study the Effect of Process Parameters on the Dimensional Deviation of Fused Deposition Modeling of 3D Printed Parts. Polymers (Basel). 2022;14(17). https://doi.org/10.3390/polym14173667

[10] Sood AK, Ohdar RK, Mahapatra SS. Parametric appraisal of mechanical property of fused deposition modelling processed parts. Mater Des. 2010;31(1):287-295. https://doi.org/10.1016/j.matdes.2009.06.016
[11] Panico A, Corvi A, Collini L, Sciancalepore C. Multi-objective optimization of FDM 3D printing parameters set via design of experiments and machine learning algorithms. Sci Rep. 2025;15:16782. https://doi.org/10.1038/s41598-025-01016-z
[12] Mohamed OA, Masood SH, Bhowmik JL. Mathematical modeling and FDM process parameters optimization using response surface methodology based on Q-optimal design. Appl Math Model. 2016;40(23-24):10052-10073. https://doi.org/10.1016/j.apm.2016.06.055
[13] Abdulrazaq M, AL-Khafaji M, Kadauw A. Mechanical Strength Optimization for the Polylactic Acid Printed Parts in Material Extrusion Process Using Artificial Neural Network. Engineering and Technology Journal. 2023;0(0):1-13. https://doi.org/10.30684/etj.2023.143270.1573
[14] Thakur A, Vates UK, Mishra S. Parametric optimization of 3D-printed PLA part using response surface methodology for mechanical properties. Smart Science. 2024;12(1):91-104. https://doi.org/10.1080/23080477.2023.2270819
[15] Fountas NA, Papantoniou I, Kechagias JD, Manolakos DE, Vaxevanidis NM. Modeling and optimization of flexural properties of FDM-processed PET-G specimens using RSM and GWO algorithm. Eng Fail Anal. 2022;138. https://doi.org/10.1016/j.engfailanal.2022.106340
[16] Almuflih AS, Abas M, Khan I, Noor S. Parametric Optimization of FDM Process for PA12-CF Parts Using Integrated Response Surface Methodology, Grey Relational Analysis, and Grey Wolf Optimization. Polymers (Basel). 2024;16(11). https://doi.org/10.3390/polym16111508
[17] Fang Q, Yu J, Shi B. Modelling and Optimisation of FDM-Printed Short Carbon Fibre-Reinforced Nylon Using CCF and RSM. Polymers (Basel). 2025;17(13). https://doi.org/10.3390/polym17131872
[18] Almansoori K, Pervaiz S. Effect of layer height, print speed and cell geometry on mechanical properties of marble PLA based 3D printed parts. Smart Materials in Manufacturing. 2023;1. https://doi.org/10.1016/j.smmf.2023.100023
[19] Jatti VS, Sapre MS, Jatti AV, Khedkar NK, Jatti VS. Mechanical Properties of 3D-Printed Components Using Fused Deposition Modeling: Optimization Using the Desirability Approach and Machine Learning Regressor. Applied System Innovation. 2022;5(6). https://doi.org/10.3390/asi5060112
[20] Anerao P, Kulkarni A, Munde Y, Kharate N. A Comparative Study of Machine Learning Techniques for Predicting Mechanical Properties of Fused Deposition Modelling (FDM)-Based 3D-Printed Wood/PLA Biocomposite. Mechanics of Advanced Composite Structures. 2025;12(2):261-270.
[21] Peko I, Čatipović N, Antunović K, Ljumović P. Multi-Objective Optimization of Fatigue Performance in FDM-Printed PLA Biopolymer Using Grey Relational Method. Sustainability (Switzerland). 2025;17(24). https://doi.org/10.3390/su172410902
[22] González González A, Zambrano-Robledo PC, Avila D, Rivas M, Quiza R. Multi-Objective Optimization of Mechanical and Geometric Properties of 3D-Printed PLA Porous Scaffolds for Biomedical Applications. Materials. 2026;19(5). https://doi.org/10.3390/ma19051008
[23] Khzzal R, Nafaa M, Hamdan W. Optimizing 3D printing parameters for PLA and PETG: advancing high-quality skull implant production. Engineering and Technology Journal. 2025;43(12):1229-1240. https://doi.org/10.30684/etj.2025.161729.1973
[24] Sapkota A, Ghimire SK, Adanur S. Fused deposition modeling (FDM) process parameter optimization for mechanical properties of 3D-printed woven fabric structures using Taguchi method. Journal of Industrial Textiles. 2025;55. https://doi.org/10.1177/15280837251339124
[25] Petousis M, Vidakis N, Mountakis N, Karapidakis E, Moutsopoulou A. Functionality Versus Sustainability for PLA in MEX 3D Printing: The Impact of Generic Process Control Factors on Flexural Response and Energy Efficiency. Polymers (Basel). 2023;15(5). https://doi.org/10.3390/polym15051232
[26] Khodaee A, Abedini V, Kami A. Effects of fused filament fabrication (FFF) process parameters on tensile and flexural properties of ABS/PLA multi-material. Journal of the Brazilian Society of Mechanical Sciences and Engineering. 2024;46(10). https://doi.org/10.1007/s40430-024-05189-y
[27] Copper3D Inc. PLACTIVE™ antibacterial nanocomposite: Technical data sheet and PLACTIVE™ Material safety data sheet (rev. Nov. 26, 2018). Santiago, Chile: Copper3D; 2018. Available from: www.copper3d.com
[28] Gonzalez YE, Mendoza JM, Durán JR, Tapia Vertel LC, Henals-Julio JD. Effect of printing parameters on mechanical properties and processing time of additively manufactured parts. Revista Materia. 2023;28(3). https://doi.org/10.1590/1517-7076-rmat-2023-0111
[29] John J, Devjani D, Ali S, Abdallah S, Pervaiz S. Optimization of 3D printed polylactic acid structures with different infill patterns using Taguchi-grey relational analysis. Advanced Industrial and Engineering Polymer Research. 2023;6(1):62-78. https://doi.org/10.1016/j.aiepr.2022.06.002

[30] Ahmad MN, et al. Application of Taguchi Method to Optimize the Parameter of Fused Deposition Modeling (FDM) Using Oil Palm Fiber Reinforced Thermoplastic Composites. Polymers (Basel). 2022;14(11). https://doi.org/10.3390/polym14112140
[31] Zonoobi MA, Haghshenas Gorgani H, Javaherneshan D. Experimental investigation and multi-objective optimization of FDM process parameters for mechanical strength, dimensional accuracy, and cost using a hybrid algorithm. Scientia Iranica. 2025;32(6).
[32] Hasan MR, Davies IJ, Pramanik A, John M, Biswas WK. Impact of process parameters on improving the performance of 3D printed recycled polylactic acid (rPLA) components. International Journal of Advanced Manufacturing Technology. 2024;131(7-8):3751-3779. https://doi.org/10.1007/s00170-024-13140-7
[33] Harishbabu S, Alrasheedi NH, Louhichi B, Sahu SK, Ma Q. Optimization and Prediction of Mechanical Properties of Additively Manufactured PLA/GNP Composites via Response Surface Methodology and Machine Learning Models. Polymers (Basel). 2025;17(21). https://doi.org/10.3390/polym17212894
[34] Linh PN, Pham VT, Tu NQ, Nguyen VC. Optimization of PLA 3D Printing Parameters using a Combined SMART-MOORA Multi-Criteria Decision-Making Approach. Engineering, Technology and Applied Science Research. 2025;15(1):19460-19465. https://doi.org/10.48084/etasr.9085
[35] Patil S, Sathish T, Makki E, Giri J. Experimental study on mechanical properties of FDM 3D printed polylactic acid fabricated parts using response surface methodology. AIP Adv. 2024;14(3). https://doi.org/10.1063/5.0191017
[36] Kartal F. Mechanical performance optimization in FFF 3D printing using Taguchi design and machine learning approach with PLA/walnut Shell composites filaments. Journal of Vinyl and Additive Technology. 2025.
[37] Sharma S, Gupta V, Mudgal D, Srivastava V. Optimization of polydopamine coating process for poly lactic acid-based 3D printed bone plates using machine learning approaches. Polym Eng Sci. 2024;64(1):279-295. https://doi.org/10.1002/pen.26546
[38] Dogan O, Kamer MS, Sahan MF. Multi-Objective Optimization of Low-Velocity Impact and Compression Behavior of 3D-Printed PLA Cubic Samples. Polymers (Basel). 2025;17(5). https://doi.org/10.3390/polym17050627
[39] Aziz MM, Beard L, Ali S, Eltaggaz A, Deiab I. Optimization Scheme for 3D Printing of PLA-PHBV-PCL Biodegradable Blends for Use in Orthopedic Casting. Polymers (Basel). 2025;17(7). https://doi.org/10.3390/polym17070852
[40] Kisin B, Turan MK, Karpat F. Multi-Objective Optimization of Biodegradable and Recyclable Composite PLA/PHA Parts. Polymers (Basel). 2025;17(15). https://doi.org/10.3390/polym17152147
[41] Antunović K, Peko I, Čatipović N, Krolo J. Multi-Objective Optimization of PLA Biopolymer FDM 3D Printing for Improved Impact Strength, Surface Quality and Production Efficiency via Grey Relational Analysis. Applied Sciences (Switzerland). 2026;16(4). https://doi.org/10.3390/app16041871
[42] Kumar K, Singh H. Multi-Objective Optimization of Fused Deposition Modeling for Mechanical Properties of Biopolymer Parts Using the Grey-Taguchi Method. Chinese Journal of Mechanical Engineering (English Edition). 2023;36(1). https://doi.org/10.1186/s10033-023-00847-z